

## Climate at high-obliquity



David Ferreira<sup>\*</sup>, John Marshall, Paul A. O’Gorman, Sara Seager

Department of Earth, Atmospheric and Planetary Science, Massachusetts Institute of Technology, Cambridge, MA 02139, United States

### ARTICLE INFO

#### Article history:

Received 2 October 2013

Revised 21 August 2014

Accepted 9 September 2014

Available online 19 September 2014

#### Keywords:

Atmospheres, dynamics

Meteorology

Earth

Extra-solar planets

Habitability

### ABSTRACT

The question of climate at high obliquity is raised in the context of both exoplanet studies (e.g. habitability) and paleoclimates studies (evidence for low-latitude glaciation during the Neoproterozoic and the “Snowball Earth” hypothesis). States of high obliquity,  $\phi$ , are distinctive in that, for  $\phi \geq 54^\circ$ , the poles receive more solar radiation in the annual mean than the equator, opposite to the present day situation. In addition, the seasonal cycle of insolation is extreme, with the poles alternatively “facing” the Sun and sheltering in the dark for months.

The novelty of our approach is to consider the role of a dynamical ocean in controlling the surface climate at high obliquity, which in turn requires understanding of the surface winds patterns when temperature gradients are reversed. To address these questions, a coupled ocean–atmosphere–sea ice GCM configured on an Aquaplanet is employed. Except for the absence of topography and modified obliquity, the set-up is Earth-like. Two large obliquities  $\phi$ ,  $54^\circ$  and  $90^\circ$ , are compared to today’s Earth value,  $\phi = 23.5^\circ$ .

Three key results emerge at high obliquity: (1) despite reversed temperature gradients, mid-latitudes surface winds are westerly and trade winds exist at the equator (as for  $\phi = 23.5^\circ$ ) although the westerlies are confined to the summer hemisphere, (2) a habitable planet is possible with mid-latitude temperatures in the range 300–280 K and (3) a stable climate state with an ice cap limited to the equatorial region is unlikely.

We clarify the dynamics behind these features (notably by an analysis of the potential vorticity structure and conditions for baroclinic instability of the atmosphere). Interestingly, we find that the absence of a stable partially glaciated state is critically linked to the absence of ocean heat transport during winter, a feature ultimately traced back to the high seasonality of baroclinic instability conditions in the atmosphere.

© 2014 Elsevier Inc. All rights reserved.

### 1. Introduction

Exoplanets, including those that have the potential to harbor life, are expected to have a range of obliquities. The reasoning is based both on the range of obliquities of the terrestrial planets of our own Solar System as well as predictions for exoplanets. The obliquity of Mars has been shown to vary chaotically, ranging from zero to nearly sixty degrees (Laskar and Robutel, 1993; Touma and Wisdom, 1993). Venus has an obliquity close to  $180^\circ$ , and therefore a retrograde rotation (Carpenter, 1964; Shapiro, 1967). While measurements of exoplanet obliquity are unlikely to be possible (but c.f. Carter and Winn, 2010 for a specialized case), the final states of exoplanet obliquity evolution will be affected by gravitational tides and thermal atmospheric tides, core–mantle friction (Correia and Laskar, 2011; Cunha et al., 2014), and collisions with other planets

or planetesimals. A large Moon is also thought to play a stabilizing role on obliquity variations, however it depends on the planet’s initial obliquity (Laskar et al., 1993). The tidal evolution depends on a planet’s distance to its host star, which for habitable zones changes for different star type. While a number of publications have addressed the influence of obliquity on climates of Earth-like planets none have considered a dynamic ocean (Gaidos and Williams, 2004; Spiegel et al., 2009; Cowan et al., 2012; Armstrong et al., 2014).

If obliquity exceeds  $54^\circ$ , polar latitudes receive more energy per unit area, in the yearly mean, than do equatorial latitudes and undergo a very pronounced seasonal cycle, a challenge for the development of life (Fig. 1 and further discussion below). A key aspect with regard to habitability is to understand how the atmosphere and ocean of this high obliquity planet work together to transport energy meridionally, mediating the warmth of the poles and the coldness of the equator. How extreme are seasonal temperature fluctuations? Should one expect to find ice around the equator?

<sup>\*</sup> Corresponding author at: Department of Meteorology, University of Reading, PO Box 243, Reading RG6 6BB, UK.

E-mail address: [d.g.ferreira@reading.ac.uk](mailto:d.g.ferreira@reading.ac.uk) (D. Ferreira).

Additional motivation for the study of climate at high obliquity is found in Earth's climate history which shows evidence of large low-latitude glaciations during the Neoproterozoic (~700–600 Myr ago). An interpretation is that Earth was completely covered with ice at these periods, the so-called “Snowball Earth” hypothesis (Kirschvink, 1992; Hoffman et al., 1998). This hypothesis raises challenging questions about the survival of life during the long (~10 Myr) glacial spells and requires an escape mechanism out of a fully glaciated Earth (see Pierrehumbert et al., 2011, for a review). An alternative to the “Snowball Earth” state is that Earth was in a high obliquity configuration with a cold equator and warm poles. The interpretation is then that large ice caps existed in equatorial regions while the poles remained ice-free. From a climate perspective (leaving aside other difficulties, see Hoffman and Schrag (2002)), it is unclear if such a climate state can be achieved in the coupled system. Recent work showed that the existence of large stable ice caps critically depends on the meridional structure of the ocean heat transport (OHT): sea ice caps extend to latitudes at which the OHT has maxima of convergence (Rose and Marshall, 2009; Ferreira et al., 2011). To address such questions, one needs to consider dynamical constraints on the ocean circulation and understand the pattern of surface winds.

High values of obliquity particularly challenge our understanding of climate dynamics because the poles will become warmer than the equator and we are led to consider a world in which the meridional temperature gradients, and associated prevailing zonal wind, have the opposite sign to the present Earth, and the equatorial Hadley circulation exists where it is cold rather than where it is warm.

The problem becomes even richer when one considers the dynamics of an ocean, should one exist. The volume and surface

area of a planet's ocean is not known a priori and is expected to be highly variable from planet to planet due to the stochastic nature of delivery of volatiles to a planet during its early phase. While the surface area of an ocean contributes to a planet's surface climate (see a series of arguments in Abe et al., 2011; Zsom et al., 2013; Kasting et al., 2013; Seager, 2014) investigating ocean surface area is beyond the scope of this paper. A deep Earth-like ocean, on the other hand, allows for a system of 3-dimensional ocean currents that is able to transport large amount of heat and mitigate harsh climates, like the Gulf Stream and Meridional Overturning Circulation (MOC) do on our present-day Earth (e.g. Seager et al., 2002; Ferreira et al., 2010). A central question for the ocean circulation is then: what is the pattern of surface winds at high obliquities?, for it is the winds that drive the ocean currents and MOC. How do atmospheric weather systems growing in the easterly sheared middle latitude jets and subject to a global angular momentum constraint, combine to determine the surface wind pattern. Should one expect middle latitude easterly winds? If not, why not?

Here, possible answers to some of these questions are sought by experimentation with a coupled atmosphere, ocean and sea-ice General Circulation Model (GCM) of an Earth-like Aquaplanet: i.e. a planet like our own but on which there is only an ocean but no land. The coupled climate is studied across a range of obliquities (23.5, 54 and 90°).

The novelty of our approach is the use of a coupled GCM in which both fluids are represented by 3d fully dynamical models. To our knowledge, previous studies of climate at high-obliquity only employed atmosphere-only GCM or atmospheric GCM coupled to a slab ocean (e.g. Jenkins, 2000; Donnadieu et al., 2002; Williams and Pollard, 2003). There, the ocean is treated as a “swamp” without OHT or with a prescribed OHT or with a diffusive OHT. Other studies are based on Energy Balance Models (EBM, see North et al. (1981, for a review) in which dynamics is absent and all (atmosphere + ocean) transports are represented through a diffusive process (e.g. Williams and Kasting, 1997; Gaidos and Williams, 2004; Spiegel et al., 2009).

In our simulations, the OHT is realized as part of the solution. Our approach allows us to document the ocean circulation at high-obliquity and to explore, in a dynamically consistent way, the role of the ocean in setting the climate. We present some of the descriptive climatology of our solutions and how they shed light on the deeper questions of coupled climate dynamics that motivate them. We focus on understanding the ocean circulation and its forcing. This leads us into a detailed analysis of the mechanisms responsible for the maintenance of surface winds. We notably elucidate the conditions for baroclinic instability and storm track development in a world with reversed temperature gradients. Our analysis of the atmospheric dynamics and energy transports are also a novelty of this study.

We use an Aquaplanet set up, a planet entirely covered with a 3000 m-deep ocean. The previous studies mentioned above used present-day and neoproterozoic continental distributions. One might be concerned by the absence of topographical constraints in our Aquaplanet. Fig. 2 however illustrates that the energy transports simulated in Aquaplanet at  $\phi = 23^\circ$  compare favorably with present-day observed transports (in terms of shape, magnitude and partitioning between ocean and atmosphere – see further discussion in Marshall et al. (2007)). That is, the main features of the ocean and atmosphere circulations of our present climate are well captured in an Aquaplanet set-up. Although continental configurations can influence the climate state and are indeed important to explain some aspects of present and past Earth's climate (Enderton and Marshall, 2009; Ferreira et al., 2010), such a level of refinement is not warranted for a first investigation of the coupled system at high obliquity.

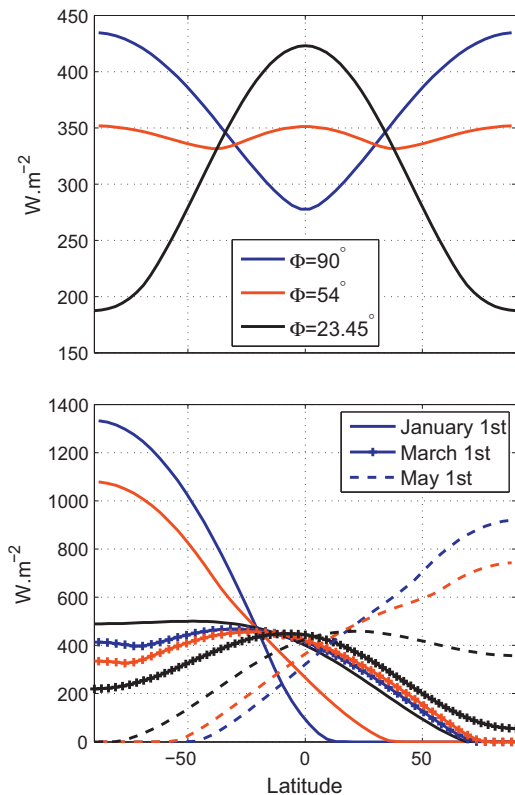


**Fig. 1.** Top-of-the-atmosphere incoming solar radiation ( $\text{W m}^{-2}$ ) for obliquities of 90° (blue), 54° (red) and 23.45° (black): (top) annual mean and (bottom) daily mean on January 1st (solid), March 1st (dotted), and May 1st (dashed). A zero eccentricity is assumed. (For interpretation of the references to color in this figure legend, the reader is referred to the web version of this article.)

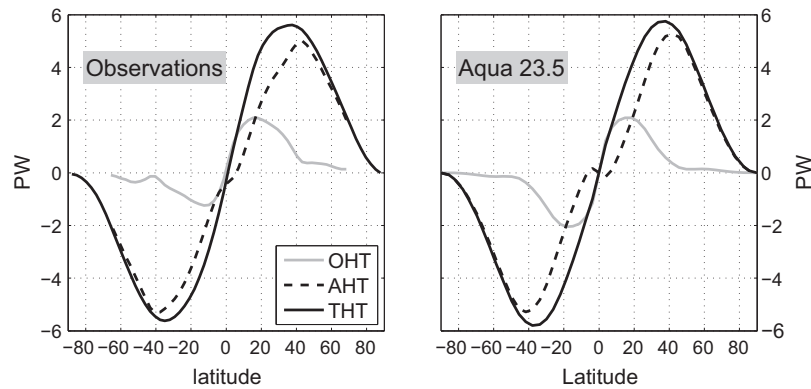


**Fig. 2.** Ocean, atmosphere and total heat transports (in  $\text{PW} = 10^{15} \text{ W}$ ) as observed on present-day Earth (left, from [Trenberth and Caron \(2001\)](#)) and in the coupled Aquaplanet GCM with a  $23.5^\circ$  obliquity (right).

A short description of our coupled GCM is given in Section 2. Section 3 focuses on the atmospheric dynamics and the maintenance of surface wind patterns. Energy transports and storage in the coupled system are described in Section 4. Implication of our results for exoplanets' habitability and Snowball Earth are discussed in Section 5. Conclusions are given in Section 6. An appendix briefly describes simulations at  $54^\circ$  obliquity.

## 2. The coupled GCM

We employ the MITgcm ([Marshall et al., 1997](#)) in a coupled ocean–atmosphere–sea ice “Aquaplanet” configuration. The model exploits an isomorphism between the ocean and atmosphere dynamics to generate an atmospheric GCM and an oceanic GCM from the same dynamic core ([Marshall et al., 2004](#)). Along with salinity (ocean) and specific humidity (atmosphere), the GCMs solve for potential temperature, the temperature that a fluid parcel would have if adiabatically returned to a reference surface pressure (traditionally expressed in Celsius in the ocean and in Kelvin in the atmosphere). All components use the same cubed-sphere grid at coarse C24 resolution ( $3.75^\circ$  at the equator), ensuring as much fidelity in model dynamics at the poles as elsewhere. The ocean component is a primitive equation non-eddy-resolving model, using the rescaled height coordinate  $z^*$  ([Adcroft et al., 2004](#)) with 15 levels and a flat bottom at 3 km depth (chosen to approximate present-day ocean volume, and thus total heat capacity). Convection is implemented as an enhanced vertical mixing of temperature and salinity ([Klinger et al., 1996](#)). Vertical background diffusivity is uniform at  $3 \times 10^{-5} \text{ m}^2 \text{ s}^{-1}$ . Effects of mesoscale eddies are parametrized as an advective process ([Gent and McWilliams, 1990, hereafter GM](#)) and an isopycnal diffusion ([Redi, 1982](#)). In the Redi scheme, temperature and salinity are diffused along surfaces of constant density, not horizontally. The GM scheme is a parametrization based on first principles: (1) it flattens isopycnal surfaces releasing available potential energy, hence mimicking baroclinic instability and (2) it is adiabatic (i.e. conserves water masses properties). In contrast to the (unphysical and deprecated) horizontal mixing scheme, these two eddy schemes capture the quasi-adiabatic nature of eddy mixing in the ocean interior and simulate an oceanic flow regime similar to that observed in our oceans. The Redi and GM eddy coefficients are both set to  $1200 \text{ m}^2 \text{ s}^{-1}$ . As for the vertical diffusivity, these values are typically observed in Earth's oceans.

The atmosphere is a 5-level<sup>1</sup> primitive equation model with moist physics based on SPEEDY ([Molteni, 2003](#)). These include a four-band long and shortwave radiation scheme with interactive

water vapor channels, diagnostic clouds, a boundary layer parameterization and mass-flux scheme for moist convection. Details of these parameterizations (substantially simpler than used in high-end models) are given in [Rose and Ferreira \(2013\)](#). Present-day atmospheric  $\text{CO}_2$  is prescribed. Insolation varies seasonally but there is no diurnal cycle (eccentricity is set to zero and the solar constant  $S_0$  to  $1366 \text{ W m}^{-2}$ ). Despite its simplicity and coarse resolution, the atmospheric component represents the main features of Earth's atmosphere, including vigorous midlatitudes synoptic eddies, an Intertropical Convergence Zone and Hadley Circulation, realistic precipitation patterns, and top-of-the-atmosphere longwave and shortwave fluxes (see [Molteni \(2003\)](#) for a detailed description).

The sea ice component is a 3-layer thermodynamic model based on [Winton \(2000\)](#) (two layers of ice plus surface snow cover). Prognostic variables include ice fraction, snow and ice thickness, and ice enthalpy accounting for brine pockets with an energy-conserving formulation. Ice surface albedo depends on temperature, snow depth and age ([Ferreira et al., 2011](#)). The model achieves machine-level conservation of heat, water and salt, enabling long integrations without numerical drift ([Campin et al., 2008](#)). The reader is referred to [Ferreira et al. \(2010\)](#) for further details about the set-up.

Integrations of the coupled system (to statistical equilibrium) are carried out for three values of obliquity  $\phi$ :  $23.5^\circ$ ,  $54^\circ$  and  $90^\circ$  (Aqua23, Aqua54, and Aqua90, respectively). All other parameters remain the same. We emphasize here that our focus is on an Earth-like coupled system, including a consistent set of parameterizations and parameter values. We do not expect our main conclusions to be very sensitive to these choices if varied within the range of observationally constrained values. However, it is conceivable that ocean and atmosphere on exoplanets sit in very different regimes than those of Earth. For example, on present-day Earth, half of the energy required for vertical mixing is provided by the dissipation of tides on the ocean floor: ocean mixing could be very different on a Moon-less planet. Exploration of such a scenario is beyond the scope of this paper.

## 3. Momentum transport: maintenance of the surface winds

### 3.1. Insolation and temperature distribution

For present-day obliquity ( $\phi = 23.5^\circ$ ), the annual-mean incoming solar radiation at the top of the atmosphere is largest at the equator and decreases by  $\sim 50\%$  toward the poles ([Fig. 1, top](#)). At  $\phi = 90^\circ$ , the pattern is reversed, with a pole-to-equator decrease of about 30%. For  $\phi = 54^\circ$ , the profile is nearly flat.

Over the seasonal cycle, all three obliquities show rather similar behaviors. The summer/winter hemisphere contrast, however, is the strongest at  $\phi = 90^\circ$  and the weakest at  $\phi = 23.45^\circ$  (and would

<sup>1</sup> Tick marks on the pressure axis of [Figs. 3 and 8](#) correspond to the mid- and interface levels of the vertical grid, respectively.

disappear for  $\phi = 0^\circ$ ). It is the amplitude of the seasonal contrast that dictates the annual mean values. At  $\phi = 23.5^\circ$ , the equator receives a steady  $\sim 400 \text{ W m}^{-2}$  throughout the year while the solar input at the poles barely reaches  $500 \text{ W m}^{-2}$  in summer and vanishes in winter. During Boreal winter at  $\phi = 90^\circ$ , the Northern Hemisphere (NH) is almost completely in the dark while the south pole receives a full  $1300 \text{ W m}^{-2}$ . In contrast, the equator oscillates between a medium solar input ( $\leq 500 \text{ W m}^{-2}$ ) and near darkness, and so has a modest annual-mean value.

Focusing on the  $90^\circ$  case, the annual-mean potential temperature distribution reflects the annual mean insolation (Fig. 3, top left): cold at the equator and warm at the poles. Interestingly, we observe a rather mild climate, with surface temperatures within a narrow range (275–295 K) and a weak Equator-to-Pole differences of 20 K. For comparison, Equator-to-Pole differences are about 30 K in Aqua23 and in the present-day climate. These annual-mean Equator-to-Pole temperature differences largely reflect the annual-mean Equator-to-Pole insolation contrast.

The climate exhibits more surprising features on a seasonal basis. In January (Fig. 4, top left), despite the long NH darkness, the north pole remains well above freezing (the minimum temperature of 285 K is reached in March) while temperatures at the south pole, receiving about  $1300 \text{ W m}^{-2}$ , “only” reach 315 K. For comparison, in a simple EBM without meridional heat transport and a small heat capacity (no ocean), Armstrong et al. (2014) find that polar temperatures at  $\phi = 90^\circ$  vary from 217 K to 389 K, a 170 K seasonal amplitude, compared to 30 K here.

In the ocean (Fig. 4), we also observe a cold equator and warm poles and in reverse to present day conditions, a large stratification is found at the pole and a weak stratification at the equator. Seasonal variations are restricted to the upper 200 m. In January, the upper ocean warms up to  $26^\circ\text{C}$  at the south pole and cools down to  $14^\circ\text{C}$  at the north pole. The equator remains at a steady  $2^\circ\text{C}$  (again well above the freezing point, about  $-1.9^\circ\text{C}$  for our salty ocean).

How are such mild annual mean temperatures and weak seasonal variations achieved at  $\phi = 90^\circ$ , despite the large incoming solar fluctuations? One can isolate three main mechanisms that ameliorate the extremes: atmospheric energy transport, oceanic energy transport and seasonal heat storage in the ocean. Fig. 5 shows the ocean, atmosphere and total energy transports. The annual transports are equatorward nearly everywhere (in opposite direction to the transports seen at  $23.5^\circ$  obliquity and on Earth, see Fig. 2), but directed down the large-scale temperature gradient. Interestingly, both ocean and atmosphere transports are essentially limited to one season. They are large during summertime and nearly vanish in winter (see for example January in Fig. 5).

Both ocean and atmosphere energy transports are a consequence of atmospheric circulation, directly in the atmosphere and indirectly in the ocean, which is of course driven by surface winds. In this context, a key question is to understand the development of synoptic scale eddies in the atmosphere. Synoptic systems facilitate these transports: in the atmosphere, they are very efficient at transporting energy while their eddy momentum fluxes also maintain the surface winds which drive the ocean:

$$\bar{\tau}_x = - \int_0^\infty \partial_y (\bar{\rho} u' v') dz \quad (1)$$

where  $\tau_x$  is the zonal surface wind stress applied to the ocean,  $\rho$  the density of air, overbars denote a time and zonal average, and primes a deviation from this average.

We now go on to explore the dynamics of the atmospheric circulation of Aqua90.

### 3.2. Development of the storm track

Since the circulation in Aqua90 is very strongly seasonal, we will focus on one month of the year, January, which corresponds to wintertime in the NH and summertime in the SH. In January, large temperature gradients ( $\sim 40 \text{ K}$ ) develop in the mid-latitudes

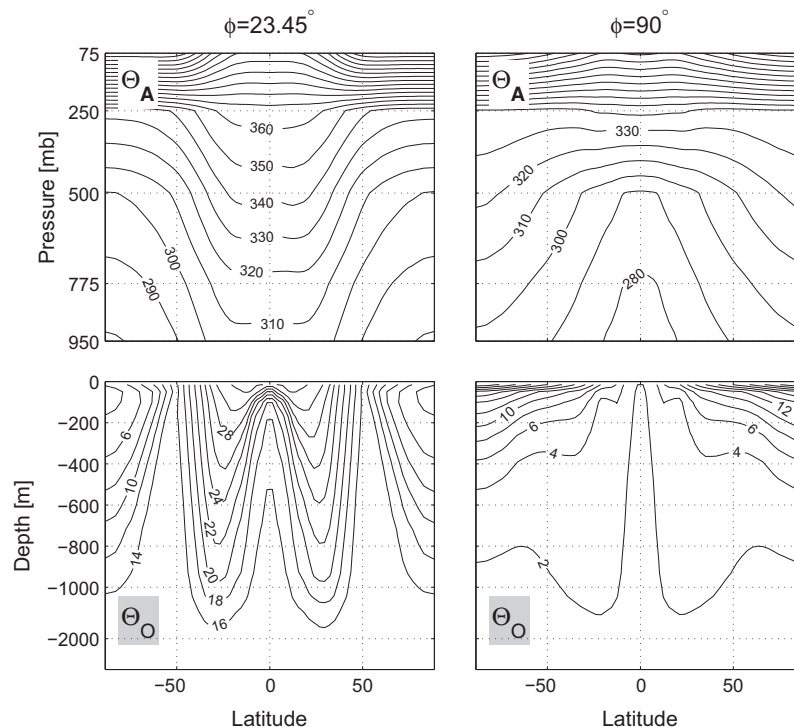


**Fig. 3.** Zonal and annual averaged atmospheric (top, in K) and oceanic (bottom, in  $^\circ\text{C}$ ) potential temperature in Aqua23 and Aqua90. Note that, in the bottom row, the upper ocean (0–1000 m) is vertically stretched.



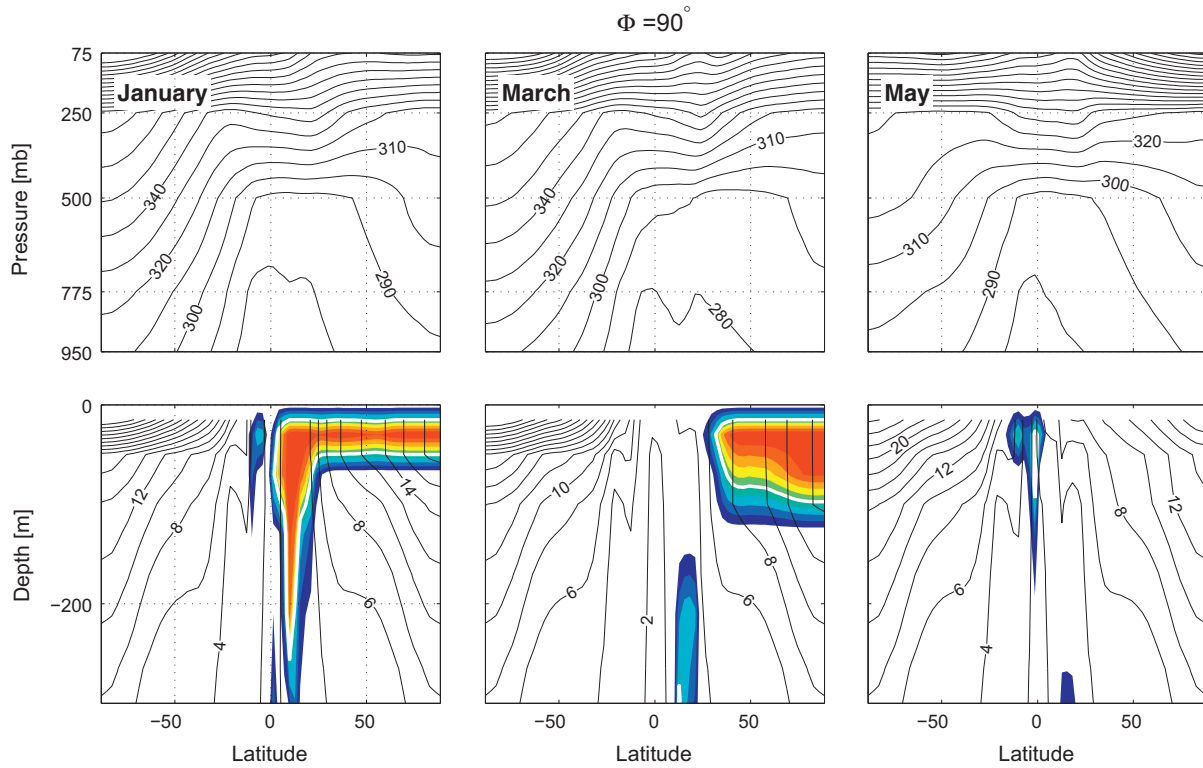


**Fig. 4.** Zonal mean potential temperature of (top) the atmosphere (in K) and (bottom) of the ocean (in °C) in Aqua90: (left) January, (middle) March, and (right) May. Color shading in the ocean denotes the presence of convection. The convective index varies between 100% (red, permanent convection) and 0% (blue, no convection at all). The white contour indicates the 50% value. (For interpretation of the references to color in this figure legend, the reader is referred to the web version of this article.)

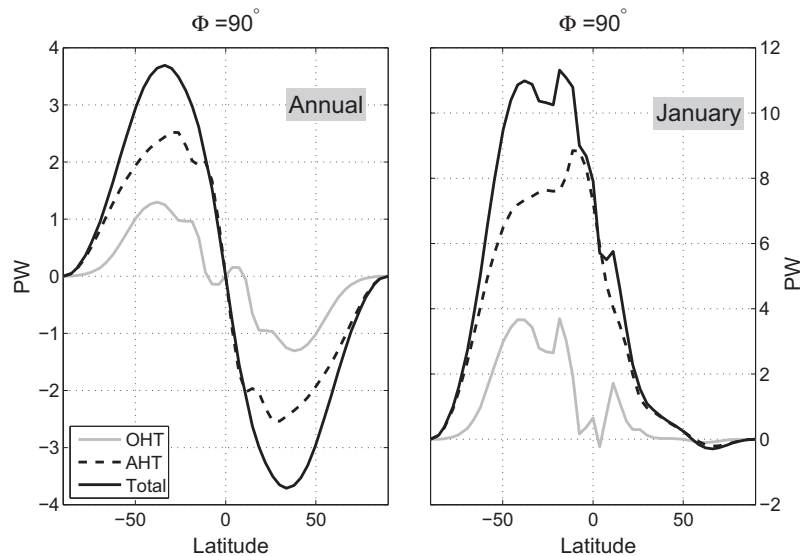


**Fig. 5.** Annual mean (left) and January mean (right) atmospheric, oceanic and total energy transports in Aqua90. Note the different ordinate scales in the two plots.

of the SH (Fig. 4, top left). In the NH, temperature gradients are very weak ( $\sim 10$  K), partly because there is little contrast of incoming solar radiation across the hemisphere (Fig. 1, bottom) and partly because the atmosphere is nearly uniformly heated from below by the ocean (see below).

To determine the propensity to baroclinic instability, we compute the meridional gradients of mean quasigeostrophic potential vorticity (QGPV)  $\bar{q}_y$ :

$$\bar{q}_y = \beta - \bar{u}_{yy} + f^2 \frac{\partial}{\partial p} \left( \frac{1}{\bar{R}} \frac{\bar{u}_p}{\bar{\theta}_p} \right) \quad (2)$$

where  $\bar{u}$  is the mean zonal wind,  $\bar{\theta}$  the mean potential temperature,  $f$  the Coriolis parameter and  $\beta$  its meridional gradient, and  $\bar{R}$  is the gas constant times  $(p/p_o)^\kappa p^{-1}$  (with  $\kappa = 2/7$  and  $p_o = 1000$  mb the reference surface pressure).

The QGPV gradient is computed on model levels and the discretization of Eq. (2) accounts for the upper and lower boundary conditions, following the approach of Smith (2007). That is, the QGPV gradient shown in Fig. 6 effectively includes a representation of the top and bottom PV sheets, as in the generalized PV definition of Bretherton (1966). In the pressure coordinate system used here, we approximate  $\omega = 0$  at the surface (the vertical velocity  $\omega$  is

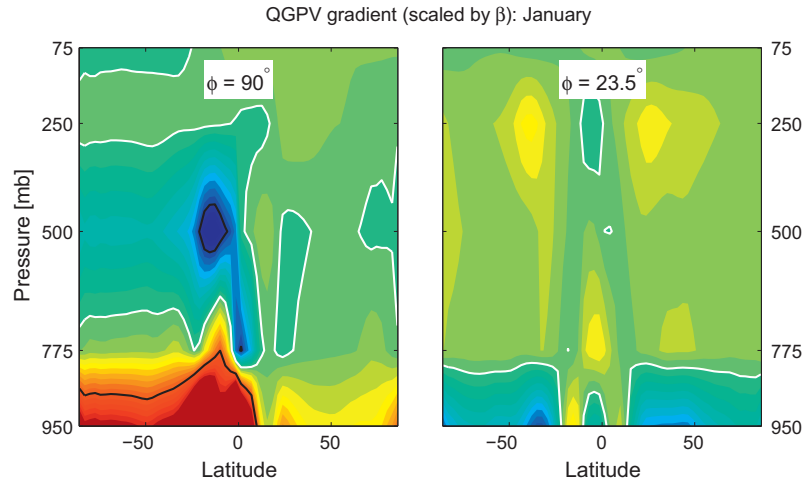


**Fig. 6.** January zonal mean meridional gradients of QGPV in (left) Aqua90 and (right) Aqua23. The gradients are scaled by the local value of  $\beta$ , the meridional gradient of the Coriolis parameter  $f$ . The contour interval is 1. The white and black contours highlight the 0 and  $\pm 10$  values, respectively.

exactly zero at the top of the atmosphere). The relative vorticity term  $\bar{u}_{yy}$  is neglected in Fig. 6 (it is only significant on scales smaller than the Rossby radius of deformation  $L_R$ , typically  $L_R \simeq 800\text{--}1000$  km): its inclusion does not change our conclusion but results in noisier plots.

In Aqua23,  $\bar{q}_y$  is negative near the surface and positive throughout the troposphere: the surface temperature gradient dominates over  $\beta$  near the surface while the stretching term (due to sheared wind) reinforces  $\beta$  aloft (see Fig. 7, top, for the zonal wind profiles). Both hemispheres exhibit a clear gradient reversal in the vertical (slightly larger in the SH) and the (necessary) condition for baroclinic instability is satisfied (Charney–Stern criteria). Storm tracks are thus expected to develop in both hemispheres. In Aqua90, however, surface temperature gradients are reversed and now reinforce the  $\beta$  contribution. Hence, surface QGPV gradients  $\bar{q}_y$  in Aqua90 are positive and large, particularly in the summer hemisphere. In the mid-troposphere, the strongly easterly sheared winds in the summer hemisphere result in a negative stretching term, large enough to overcome  $\beta$ . There is a clear (and ample) gradient reversal in the SH. In contrast, in the NH, where temperature gradients and wind shear are weak,  $\bar{q}_y$  is one-signed and dominated by  $\beta$  (except close to the surface where both  $\beta$  and the surface temperature contribution combine). We thus expect a storm track to develop in the SH, but not in the NH.

This is indeed the case as shown by the Reynolds stresses  $\overline{u'v'}$  developing near  $30\text{--}40^\circ\text{S}$  in January (Fig. 7, top left) and the large eddy heat flux in the atmosphere at these latitudes (Fig. 9, bottom). The presence of a storm track is also revealed by large-scale precipitation in the mid-latitudes (due to the equatorward advection in synoptic eddies of warm–moist air parcels toward the cold Equator, see Fig. 8, bottom).

The negative Reynolds stresses in the SH can be interpreted as due to Rossby waves propagating away from the baroclinically unstable zone into the Tropics (see Held, 2000). Consistent with Eq. (1), the eddy momentum convergence sustains surface westerly winds near  $50^\circ\text{S}$  and trades winds in the deep tropics (Fig. 7).

It is interesting to contrast Aqua90's stability properties with those of Aqua23. Consistent with the QGPV analysis above, storm-tracks are co-existing in summer and winter hemispheres, as evidenced by the large (poleward) eddy momentum fluxes in both hemispheres (Fig. 7 top right). As a consequence, surface westerly winds are sustained in the midlatitudes at all seasons, as well as a sizable eddy energy transport (not shown). The persistence of surface winds is key for understanding the oceanic temperature

structure (see below). In Aqua90, surface winds vanish in winter because there are no eddies to sustain them.

In Aqua90, the atmospheric meridional overturning circulation in January (Fig. 8, top) is thermally direct as in Aqua23 (upwelling in the summer/southern hemisphere and downwelling in the winter/northern hemisphere),<sup>2</sup> but has an hemispheric latitudinal extent. This circulation is likely the result of the merging of the Ferrel and Hadley cells. The Ferrel cell is expected to be clockwise given the sense of the eddy momentum fluxes in the upper troposphere (Fig. 7, upper left). Meanwhile, the Hadley cell in the SH is expected to be reversed (compared to the low obliquity case) because of the reversed temperature gradient. As a result, the two cells circulate in the same sense and appear as one single cell. In July, the upwelling branch approaches the north pole and the overturning cell is of counterclockwise from  $5^\circ\text{S}$  to  $70^\circ\text{N}$  (not shown).

## 4. Energy transports and storage

### 4.1. The ocean and atmosphere energy transports

In Aqua90, the ocean and atmosphere both transport energy northward in January, i.e. from the summer to the winter hemisphere and down the large-scale temperature gradient. This is readily rationalized following the previous analysis in Section 3.

The decomposition of the AHT into mean and eddy components is shown in Fig. 9. In January (bottom), both components are northward nearly everywhere, from the warm into the cold hemisphere. The large eddy heat flux in the SH and near zero flux in the NH are consistent with the development of baroclinic instability in the summer hemisphere only. The down-gradient direction of the flux is associated with the extraction of available potential energy from the mean flow. The eddy heat flux peaks near  $50^\circ\text{S}$  at 5 PW, a value comparable to that seen in Aqua23 (although in the latter case eddy heat fluxes exist in both hemispheres).

The transport due to the mean flow (largely the axisymmetric Hadley circulation as there is no stationary wave component in our calculations) accounts for most of the atmospheric heat transport in the tropics and all of it in the Northern Hemisphere. Even at the latitudes of the storm track the mean component is not negligible. This is in contrast with Aqua23 where the mean flow contribution to AHT is small everywhere except in the deep tropics.

<sup>2</sup> The jump of the Hadley circulation out of the boundary layer between  $5^\circ\text{S}$  and  $0^\circ$  may be explained by the mechanism of Pauluis (2004).

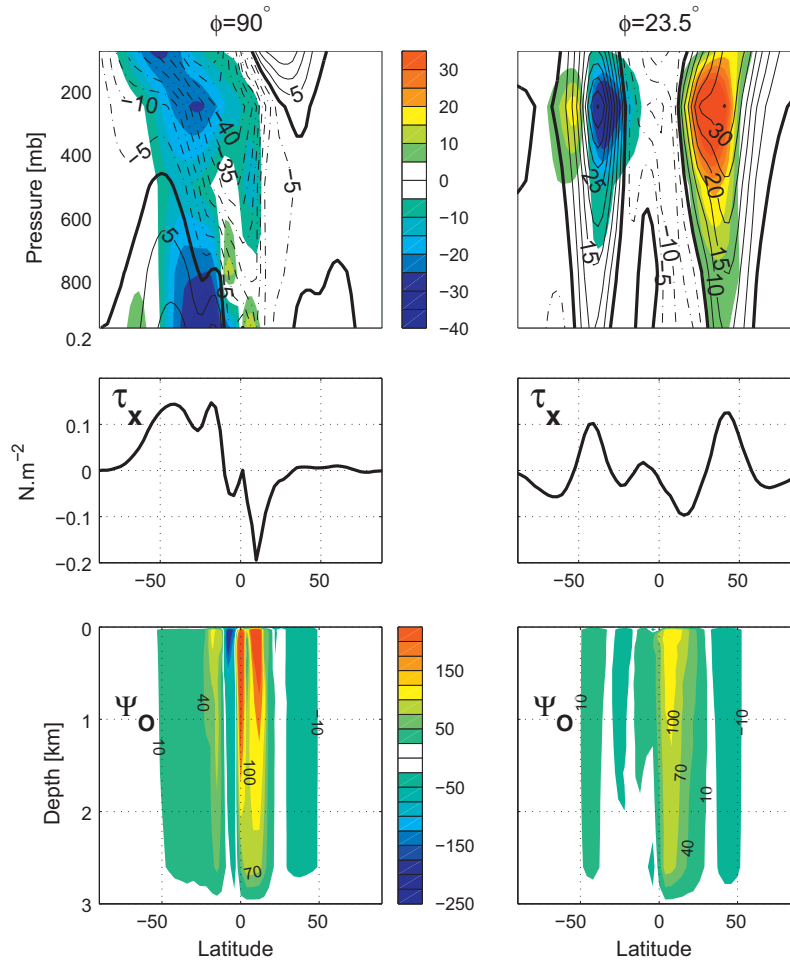


**Fig. 7.** (Top) Zonal mean zonal wind (contours, in  $\text{m s}^{-1}$ ) and Reynolds stresses (shading, in  $\text{m}^2 \text{s}^{-2}$ ), (middle) zonal mean surface wind stress (in  $\text{N m}^{-2}$ ), and (bottom) oceanic Eulerian overturning streamfunction (in Sv) in January in (left) Aqua90 and (right) Aqua23.

Note that the AHT associated with the Hadley circulation has a strong symmetry around the equator. Therefore, the July (not shown) and January Hadley cell transports largely oppose one another. In the annual mean, the mean circulation contribution nearly cancels out and the AHT is dominated by the eddy flux transport (Fig. 9, top).

The January OHT also transports heat from the pole toward the equator (Fig. 5). It is dominated by the contribution from mean Eulerian currents (not shown). The Eulerian overturning (Fig. 7, bottom left) consist of a series of Ekman wind-driven cells matching the surface wind pattern (middle). The OHT achieved by such circulation is well captured by the scaling  $\text{OHT} \sim \rho_o C_p \Delta T \Psi$  where  $\Psi$  is the strength of the circulation (in Sv), and  $\Delta T$  is the vertical gradient of temperature (see Czaja and Marshall, 2006). The clockwise circulation between  $0^\circ$  and  $25^\circ\text{N}$  is very intense, reaching up to 400 Sv. However, because it acts on a very weak vertical temperature difference  $\Delta T \sim 0$  (see Fig. 4 bottom), its contribution to the OHT is small (similarly for the cell between  $5^\circ\text{S}$  and  $0^\circ$ ). The SH midlatitude MOC cell is relatively weak ( $\sim 15$  Sv), but acts on a strong vertical gradient (notably sustained by the intense surface solar radiation). As the surface warm waters are pushed equatorward by the winds and replaced by upwelling of cold equatorial deep water, the OHT achieved by the mid-latitude wind driven cell is equatorward, close to 4 PW (Fig. 5).

It is interesting to note that the (parameterized) eddy-induced transports in the ocean are negligible outside the deep tropics (not shown). This is not the case in Aqua23 where eddy processes

are order one in the momentum and heat balance of the ocean (see Marshall et al., 2007). The absence of a significant eddy transport in Aqua90 is a consequence of the small slope of isopycnal surfaces<sup>3</sup> (except close to the equator, see Figs. 3 and 4). In comparison, steeply tilted isopycnals extend to a depth of 1000 m or more in Aqua23 (Fig. 3, bottom). The thermocline structure reflects the near permanent pattern of surface winds (polar easterlies, midlatitudes westerlies, trade winds) and associated Ekman pumping/suction. In Aqua90, surface winds come and go seasonally, disallowing the building of a permanent thermocline: isopycnal surfaces remain relatively flat.

In Aqua90 as in Aqua23, the AHT has a broad hemispheric shape, peaking in the mid-latitudes (compare Figs. 2 and 5). In Aqua23 (as in observations), the OHT is large in the subtropics decreasing poleward, with large convergences in the midlatitudes. It has a distinctly different shape from that of the AHT. In Aqua90 however, the OHT is a “scaled down (by a factor 2) version” of AHT (on the seasonal and annual timescales) and has an hemispheric extent. In January, the OHT in Aqua90 converges at the equator and vanishes in the Northern/winter hemisphere.

<sup>3</sup> To contrast with the previous discussion of PV gradients in the atmosphere, note that the eddy parameterization of Gent and McWilliams (1990) used here is not based on PV mixing (although it approximates it under some assumptions). Rather, it presupposes and represents release of available potential energy stored in tilting isopycnal surfaces.

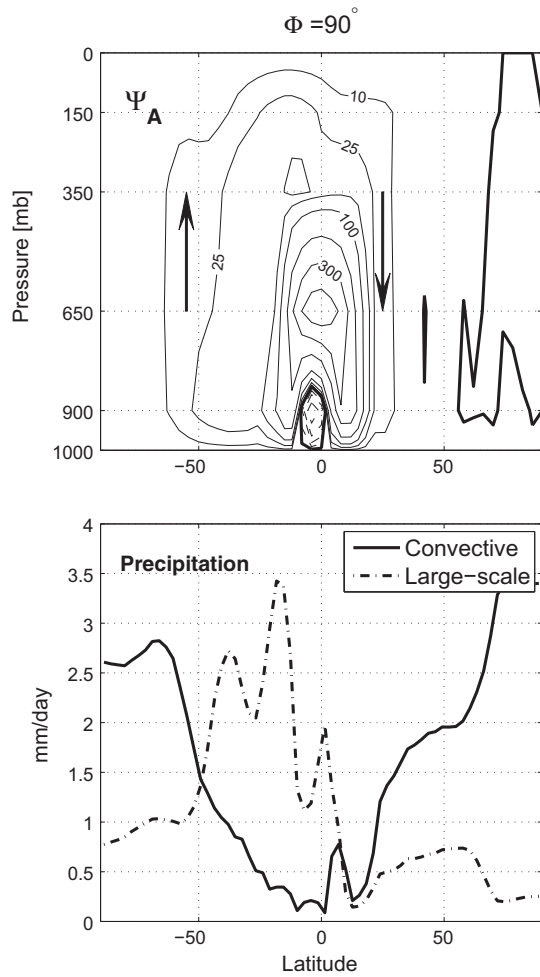


**Fig. 8.** January mean (top) Atmospheric overturning streamfunction in “atmospheric Sverdrup” ( $1 \text{ Sv} = 10^9 \text{ kg s}^{-1}$ ) and (bottom) convective and large scale precipitation (in  $\text{mm day}^{-1}$ ) in Aqua90.

#### 4.2. Ocean heat storage

The upper ocean also contributes in modulating seasonal extremes of temperature through seasonal storage of heat. In summer the ocean stores large amounts of heat, mostly by absorbing shortwave radiation, and thus delaying the increase of surface temperatures through the summer. As a consequence, the summer hemisphere upper ocean is strongly stratified (Fig. 4).

In winter, heat stored in summer is released to the atmosphere. Large amounts of heat are accessed through ocean convection which occupies the entire northern hemisphere in January and much of it in March (note also the deepening of the convective mixing as winter progresses, Fig. 4). The heating of the atmosphere from below is reflected in the fact that precipitation is largely of convective origin in the winter hemisphere (an effect probably amplified by the lack of stabilizing atmospheric eddies, Fig. 8, bottom). As a result, the atmosphere is effectively heated from below during winter. The solar heating is very weak (less than  $10 \text{ W m}^{-2}$  north of  $25^\circ\text{N}$ , see Fig. 10) while the top-of-the-atmosphere longwave cooling is nearly uniform at about  $240 \text{ W m}^{-2}$ . This cooling is almost exactly balanced by air–sea fluxes ( $\sim 220 \text{ W m}^{-2}$ , mostly due, in equal fraction, to latent heat release and longwave emission from the ocean surface, see Fig. 10, left).

The ocean plays a role in ameliorating temperature swings in two ways: (1) it supplements the AHT by transporting energy from the summer to the winter hemisphere and (2) it stores heat in

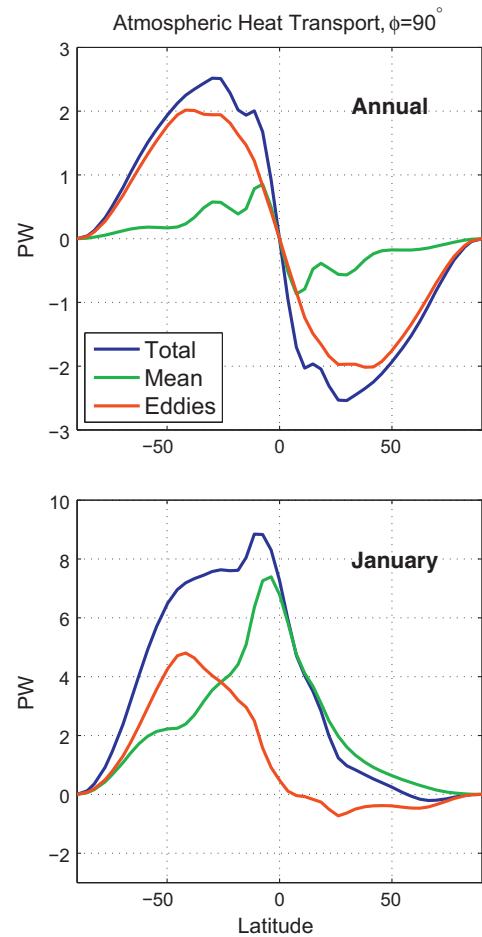


**Fig. 9.** Decomposition of the atmospheric energy transport AHT into mean and eddy components for the annual mean (top) and January mean (bottom) in Aqua90. Eddies are defined with respect to a zonal and time (monthly) mean. The annual mean eddy contribution is the average of the monthly eddy heat transports.

summer and releases it to the atmosphere in winter. What is the relative contribution of these two effects?

To compare them, we compute the OHT implied by the net air–sea heat fluxes, i.e. the meridional (and zonal) integral of the air–sea heat fluxes (starting from the north pole here). The difference between the actual and implied OHTs would be zero if there was no ocean heat storage (and indeed, on annual average, the two quantities are identical – not shown). In January (Fig. 10, right), the implied OHT reaches  $50 \text{ PW}$  at  $20^\circ\text{S}$ , that is  $50 \text{ PW}$  of heat are transferred from the atmosphere into the ocean south of  $20^\circ\text{S}$  and from the ocean into the atmosphere north of it. Clearly, only a small fraction ( $4 \text{ PW}$ , less than  $10\%$ )<sup>4</sup> of the air–sea flux is transported meridionally by the OHT, the remaining  $90\%$  being stored locally to be released the following season. In fact, even the AHT appears to play a secondary role on seasonal timescales. Within each hemisphere, the coupled ocean–atmosphere system behaves as a 1d column, storing and releasing heat over the seasonal cycle.

## 5. Implications

### 5.1. Habitability: the role of the ocean

The surface climates of  $90^\circ$  and  $54^\circ$  obliquity planets are mild, in fact milder than in Aqua23, a surprising result in perspective of the

<sup>4</sup> In Aqua23, this fraction is substantially larger, about  $30\%$  (an OHT of  $7 \text{ PW}$  for an implied OHT of  $20 \text{ PW}$ ) although the ocean heat storage remains the dominant effect.



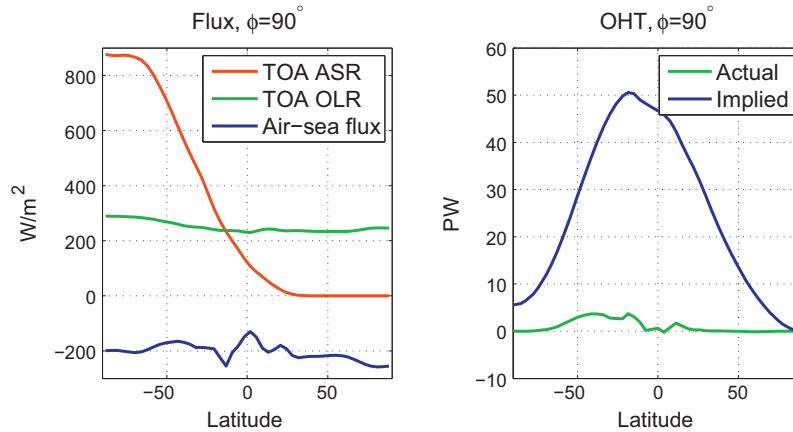


**Fig. 10.** (Left) Top-of-the-atmosphere absorbed shortwave radiation (red), out-going longwave radiation (green) and surface cooling flux (blue). The latter includes the latent heat, net longwave radiation and sensible heat at the air-sea interface, all three terms cool the surface of the ocean. (Right) Actual OHT (green) and OHT implied by the net surface heat flux (blue) in Aqua90 in January. Note that the January OHT is identical to that shown in Fig. 5 (left). (For interpretation of the references to color in this figure legend, the reader is referred to the web version of this article.)

extreme summer insolation/long polar nights at high obliquity. These conclusions are similar to those of previous studies employing atmospheric GCMs coupled to 'swamp' ocean models, i.e. a motionless ocean without OHT (Jenkins, 2000; Williams and Pollard, 2003). This is expected from our analysis in Section 4: the storage capability of the ocean largely overwhelms its dynamical contribution, the OHT.

To confirm this, we couple the atmospheric component of our coupled GCM to a "swamp" ocean. Three experiments at 90° obliquity are carried out with mixed layer depths of 10, 50 and 200 m, all initialized with uniform SST at 15 °C. Here we explore the extreme short timescale temperature fluctuations.

Statistics of the Surface Air Temperature (SAT) over the southern hemisphere polar cap (90–55°S) are shown in Fig. 11 for the slab-ocean and coupled experiments. For each month of the year, the monthly-mean SAT averaged over the polar cap (90–55°S) is plotted along with typical extreme values. The latter are the averages (over 20 years) of the minimum and maximum values reached within a given month over the polar cap. This gives a sense of the temperature fluctuations generated by weather systems for each month of the year.

As seen previously, seasonal temperature changes in the coupled system are mild. We also observed that temperature fluctuations within a given month are also relatively small: the largest fluctuations are found in summer with day-to-day changes of 20 °C (in January). Slab-ocean simulations with 50 and 200 m mixed-layer depth exhibit SAT statistics similar to those seen in the coupled GCM. The case of a 10 m deep slab ocean is remarkable as it shows a collapse in a near Snowball state. This is obviously a catastrophic outcome for habitability (see further discussion below).

The 50 and 200 m deep cases noticeably differ from the coupled system on two aspects. First, minimum wintertime temperatures are higher with a slab ocean. This is probably because a slab ocean is more efficient at storing heat in the summer because it has no compensating OHT toward the Equator. As a result, slab-ocean runs exhibit even weaker seasonal fluctuations than the coupled system. Second, the magnitude of day-to-day fluctuations increase with slab oceans (35 °C at 50 m depth). This is to be expected as temperature changes in a dynamical ocean are damped by advection by the mean currents, fluctuations in Ekman currents, upper ocean convection etc.

Although effects of a dynamical ocean are noticeable on SAT statistics, the slab-ocean simulations closely reproduce the surface climate of the coupled simulation, provided that the ocean is deep

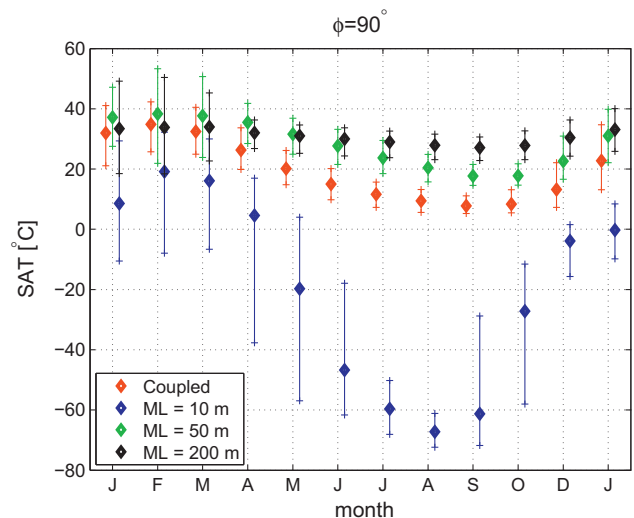


**Fig. 11.** Mean (diamond) and extreme (+) SAT in the coupled GCM and in the atmosphere-slab ocean runs for each month of the year (compiled over a 20 year period) for the Southern high-latitudes (90°S–55°S). All simulations uses  $\phi = 90^\circ$ .

enough to avoid a Snowball collapse. In an exoplanet context, in which the volume of ocean could be considered as a free parameter, our simulations suggest that the range of oceanic depths that are critical to climate is rather small, say 0 to 100 m (i.e. a water column with a heat capacity up to 100 times that of an atmospheric column for our Earth-like set up). Depth variations beyond these values would only result in small adjustments to the habitability.

## 5.2. Collapse into a completely ice-covered state

We showed in previous works that the coupled Aquaplanet at 23.5° of obliquity can support a cold state with large ice caps extending from the poles into the mid-latitudes and ice-free equatorial regions (Ferreira et al., 2011). An analogous state at high-obliquity would present an ice cap around the equator extending poleward into the mid-latitudes and ice free poles. Such a state of limited glaciation would avoid the challenges of a complete "Snowball Earth" (e.g. the survival of life, an escape mechanism). Is such a state possible?

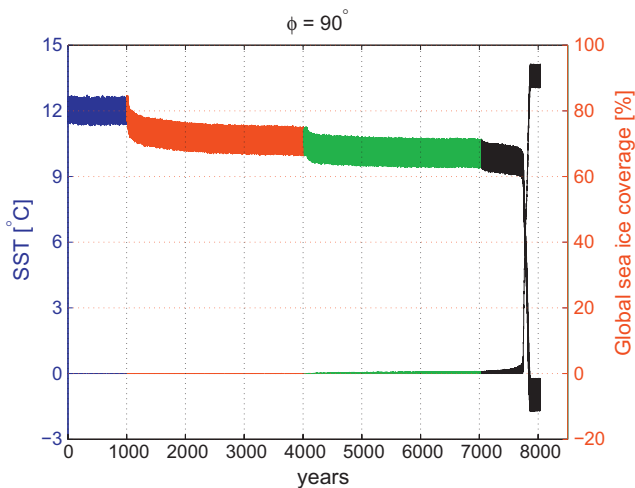


**Fig. 12.** SST (in °C, upper curve, left axis) and fraction of the globe covered with sea ice (in %, lower curve, right axis) in Aqua90 as the solar constant  $S_0/4$  is decreased from 341.5 (blue) to 339.5 (red), 338.5 (green) and 338.0 (black)  $\text{W m}^{-2}$ .

To search for this solution, we carry out an experiment in which the solar constant is lowered by small increments starting from the Aqua90 state described previously. Lowering of the solar constant results in small cooling until a dramatic global cooling for  $S_0/4 = 338 \text{ W m}^{-2}$ . At the transition, the sea ice cover jumps, within a century, from 2% of the global area to 90% and stabilizes around this value (Fig. 12). In the latter state, ice is present at all latitudes: the globally averaged 90% ice coverage is only due to somewhat reduced ( $\sim 75\%$ ) ice concentrations around the poles. In other words, we do not observe an intermediate state with a partial glaciation.

Interestingly, the same behavior is observed in the slab-ocean model. While the solutions with 200 and 50 m deep mixed-layer converges to temperate ice-free solution, the 10 m deep slab-ocean simulation collapsed into a near-complete Snowball state (Fig. 11). Note that, a 50 m mixed-layer simulation initialized with uniformly cold temperatures ( $5^\circ\text{C}$ ) similarly collapses in a Snowball state. As in the fully ice-covered state of the coupled model, above freezing temperatures and partial sea ice coverage ( $\sim 75\%$ ) are found at the poles in the summer because of the intense shortwave radiation. These results are consistent with simulations by Jenkins (2000) and Donnadieu et al. (2002) with atmospheric GCMs coupled to slab oceans. For various choices of atmospheric  $\text{CO}_2$ , solar constant and high obliquity, Jenkins (2000) observed mild climates or Snowball collapse. In Donnadieu et al. (2002), simulations with realistic configurations initialized from ice-free states rapidly converged to nearly global glaciations.<sup>5</sup>

In the context of existence of multiple climate equilibria, we showed that a large ice cap solution in Aqua23 is possible because of the meridional structure of the OHT which peaks around  $20^\circ\text{N/S}$  to decrease sharply poleward (see Fig. 2). The associated OHT convergence can stop the expansion of sea ice into the mid-latitude, notably in winter (not shown), thus avoiding the collapse into a

<sup>5</sup> In both studies as in our slab and coupled simulations, summer ice concentration near the poles is below 100%. Note however that, in our simulations the sea ice thickness (which is not artificially limited) continues to increase rapidly, even as the sea ice area is equilibrated, to reach tens of meter within 200 years. Simulations of a steady state would require taking geothermal heating into account. This is beyond the scope of this paper: it is likely however that ice would grow hundreds of meter thick (for typical geothermal flux) and that ice flows would eventually enclose the globe into a hard Snowball state.

Snowball state (see also Poulsen and Jacob, 2004; Rose and Marshall, 2009). It is therefore not surprising that slab ocean configurations without OHT would exhibit either ice-free states or near global glaciations. As soon as sea ice appears even in very small amount (2% of the global cover here), there is no mechanism to stop the sea-ice albedo feedback. This also explains why shallow slab oceans are more susceptible to global glaciations: their small thermal inertia makes it comparatively easier to approach the freezing point within a winter season and initiate the ice-albedo feedback.

But, why does the dynamical ocean behave like a swamp? This answer can be traced back to the seasonality of the storm track activity and surface wind field. As discussed in Sections 3 and 4, there are virtually no wind stress and no OHT in the winter hemisphere (see Figs. 5 and 7). In other words, when it matters the most, in winter during sea ice expansion, the dynamical ocean does behave like a swamp. Interestingly, even the extremely large heat capacity of the coupled ocean (3000 m deep) is not sufficient to stop the sea ice expansion. This is probably because just before collapse ( $\sim 7500$  years, Fig. 12) most of the deep ocean is filled with near freezing waters from the equator where a small cover of ice is present.

### 5.3. Implication for the use of EBMs

An interesting result of our simulations is that the total energy transport (THT) in the coupled system is directed down the large-scale temperature gradient at the three obliquities explored here. This occurs despite the opposite temperature gradients found at  $23.5^\circ$  and  $90^\circ$  obliquities. At  $54^\circ$  obliquity, both temperature gradients and THT are nearly vanishing, but the tropics are slightly warmer than the poles and the THT is indeed poleward.

Our calculations suggest that the use of EBMs in which energy transports are parametrized as down-gradient diffusive processes is justified (Spiegel et al., 2009). This is important as the computationally inexpensive EBMs permit to explore a wide range of parameters which would not otherwise be accessible with a full 3d coupled GCM.

There is however an important limitation: the transport efficiency,  $D$ , relating the THT to the meridional temperature gradient is not a constant, but is itself a function of the climate. This parameter is often considered as a tuning parameter and chosen to obtain a good fit to Earth's present-day climate (e.g. Williams and Kasting, 1997). Fig. 13 shows scatter plots of the THT and surface temperature gradients for our Aquaplanets simulations. Estimates (through linear fit) of  $D$  at  $90^\circ$  and  $23^\circ$  obliquity are rather similar, about  $0.7\text{--}0.8 \text{ W m}^{-2} \text{ K}^{-1}$ .<sup>6</sup> At  $\phi = 54^\circ$ ,  $D$  is substantially weaker,  $0.15 \text{ W m}^{-2} \text{ K}^{-1}$ . This is not surprising: a significant fraction of the THT is due to synoptic eddies in the atmosphere spawned by baroclinic instability which is itself sustained by the large-scale meridional temperature gradient. Starting with Green (1970) and Stone (1972), there is a large literature linking the eddy diffusivity to the meridional temperature gradient. In Aqua54, the latter is indeed much weaker than in Aqua23 and Aqua90.

This is beyond the scope of the paper to investigate the detailed relationship between the THT and temperature gradients. We emphasize here, that even in our simple Aquaplanet set-ups, the heat efficiency  $D$  varies by more than a factor 5 across climates. Sensitivities of the results to the choice of  $D$  should be explored when using EBMs.

<sup>6</sup> These values are slightly larger than those typically found in the literature for a Earth's fit,  $D \sim 0.4\text{--}0.6 \text{ W m}^{-2} \text{ K}^{-1}$ , possibly because of the absence of sea ice in our simulations. Estimates of  $D$  in colder Aquaplanet configurations with ice-covered poles give  $D \approx 0.5 \text{ W m}^{-2} \text{ K}^{-1}$ .

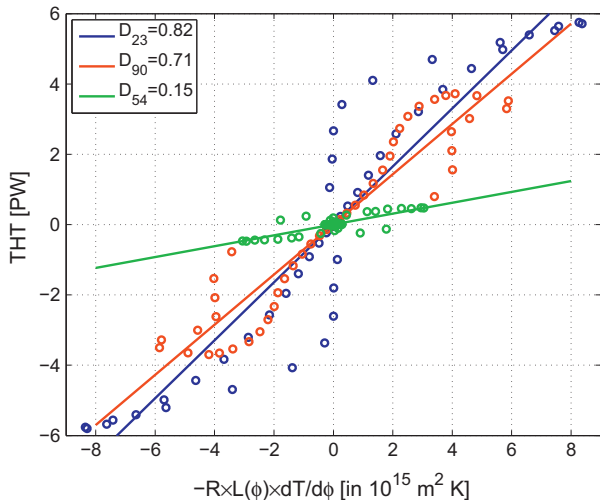


**Fig. 13.** Scatter plots of the annual-mean THT against the scaled meridional gradient of SAT,  $RL(\phi)dT/d\phi$  where  $R = 6370$  km is the radius of Earth and  $L(\phi)$  the length of a latitudinal circle at latitude  $\phi$  for (blue) Aqua23, (red) Aqua90, and (green) Aqua54. Different points correspond to different latitudes. Best linear fits are also shown in solid lines and the estimated slopes  $D$  in the upper left box. The coefficient  $D$  is expressed in  $\text{W m}^{-2} \text{K}^{-1}$  and is comparable to the heat diffusion parameter used in EBMs (North et al., 1981). (For interpretation of the references to color in this figure legend, the reader is referred to the web version of this article.)

## 6. Conclusion

We explore the climate of an Earth-like Aquaplanet with high obliquity in a coupled ocean–atmosphere–sea–ice system. For obliquities larger than  $54^\circ$ , the TOA incoming solar radiation is higher at the poles than at the equator in annual mean. In addition, its seasonality is very large compared to that found for Earth’s present-day obliquity,  $\sim 23.5^\circ$ .

At  $90^\circ$  obliquity, we find that at all seasons the equator is the coldest place on the globe and temperatures increase toward the poles. Importantly, the reversed temperature gradients, in thermal wind balance with easterly sheared winds, are large in the summer hemisphere but nearly vanish in the winter hemisphere. This largely reflects the strong gradient of TOA incoming solar radiation in the summer hemisphere but uniform darkness of the winter hemisphere. This is also because the winter atmosphere is uniformly heated by the ocean.

As a consequence, the baroclinic zone and storm track activity are confined to the midlatitudes of the summer hemisphere. Eddy momentum fluxes associated with the propagation of Rossby wave out of the baroclinic zone maintain surface westerly wind in the midlatitudes of the summer hemisphere. Conversely, surface winds nearly vanish in the winter hemisphere. This is in contrast with the  $23.5^\circ$  obliquity Aquaplanet (and present-day Earth) where storm track activity and surface westerly winds are permanent in the midlatitudes of the two hemispheres (although weaker in the summer one). The ocean circulation is dominated by its wind-driven component, and is therefore also confined to the summer hemisphere too. In the winter hemisphere, the ocean is motionless. However, heat stored during the summer in the upper ocean is accessed through convection and released to the atmosphere.

Importantly, at large obliquities, both ocean and atmosphere transport energy toward the equator but down the large-scale temperature gradient, as at low obliquities. Similarly to the circulation patterns, these transports are essentially seasonal, large in summer and vanishingly small in winter. In the atmosphere, the transport is achieved by a combination of baroclinic eddies and overturning circulation (which comprises a single cell, extending from  $60^\circ$  in the summer hemisphere to  $25^\circ$ ). In the ocean, crucially, the heat trans-

port is carried mainly by the wind-driven circulation. It worth emphasizing that, although the energy transport of the coupled system is always down-gradient in our simulations, the transport efficiency (relating the transport to the temperature gradient as is done in EBMs) is not a constant but varies by a factor 5 across climates.

As found in previous studies (e.g. Jenkins, 2000; Williams and Pollard, 2003), the surface climate at high obliquities can be relatively mild, provided collapse into a Snowball is avoided. In this case, temperatures at the poles in our Aquaplanet oscillate between 285 and 315 K, clearly in the habitable range. This is primarily explained by the large heat capacity of the surface ocean which stores heat during the summer and releases it to the atmosphere in winter. Although the OHT is substantial and down-gradient, it is of secondary importance in mitigating extreme temperature when compared to the storage effect. This is confirmed by simulations in which the dynamical ocean of our coupled GCM is replaced by a motionless ‘swamp’ ocean.

We found that Snowball collapse is possible whether a dynamical ocean with OHT or a ‘swamp’ ocean is used. Importantly, we could not find ‘intermediate’ climate state in which a substantial ice cover is present without a global coverage. This is despite expectations that a dynamical ocean could stabilize the ice margin in the midlatitudes (Poulsen et al., 2001; Poulsen and Jacob, 2004; Ferreira et al., 2011). In these studies (all at present-day obliquity), the large OHT convergence in midlatitudes (due to the wind-driven circulation) can stop the progression of the sea ice toward the equator. In our coupled simulations at high obliquity however, the OHT vanish in the winter hemisphere at the time of sea ice expansion because surface winds vanish too. This explains the similarity of the coupled GCM and swamp ocean simulations. Our results suggest that a state of high obliquity is not an alternative to the ‘Snowball Earth’ hypothesis to explain evidence of low-latitude glaciations during the neoproterozoic.

Our simulations employ a configuration without any land. Although it reproduces (at  $23.5^\circ$  obliquity) the main features of present day climate, it is plausible that particular continental configurations would have a first order impact on the climate, for example in cases where large areas of land are removed from all oceanic influences (e.g. a large polar continent). In such cases, only the atmospheric heat transport could modulate the extreme seasonal fluctuations, possibly resulting in temperature excursions beyond the habitability range. Similarly, we reiterate that we explore here an Earth-like ocean–atmosphere–sea ice system. We believe that our results are robust to small changes in parameters around the Earth-like choice used here (say doubling/halving of eddy diffusion coefficient, rotation rate, etc). Significant deviation from these values however would require further investigation.

Keeping these limitations in mind, it appears that a dynamical ocean makes little difference whether one is interested in the habitability of exoplanets or paleoclimate. This suggests that inferences made from simulations using a ‘swamp’ ocean with no OHT at high obliquity are robust (e.g. Jenkins, 2000, 2003; Donnadieu et al., 2002; Williams and Pollard, 2003). Two caveats should be noted. First, this conclusion results from the strong seasonality of the surface winds, itself the consequence of complex atmospheric dynamics (conditions for baroclinic instability). This conclusion should not be extended to other situations without caution. Secondly, although ‘swamp’ ocean formulation appears to perform similarly to a fully dynamical ocean, they rely on an ad hoc choice of a mixed layer depth. In reality, the depth of the mixed layer is a function of space and time and is determined by ocean dynamics and air–sea interactions. Unfortunately, the choice of the mixed layer depth has a direct impact on the solution. In our set-ups, ice-free or Snowball states can be obtained depending on this choice (with multiple solutions possible for a 50 m deep mixed layer). This is worth keeping in mind when carrying out such simulations.

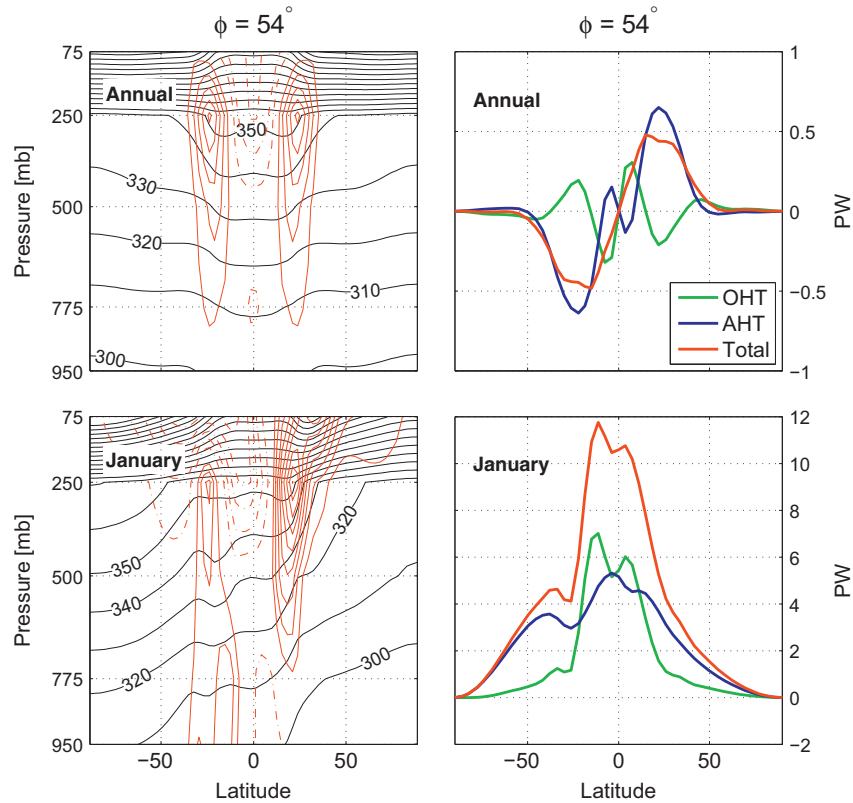


**Fig. 14.** Aqua54 simulation: (left) potential temperature (K) and zonal mean wind ( $\text{m s}^{-1}$ ) and (right) oceanic, atmospheric and total energy transports. Annual and January averages are shown at the top and bottom, respectively.

## Appendix A. Climate at 54° obliquity

On seasonal scales, atmospheric and oceanic circulations in Aqua54 show many similarities with those seen at 90° obliquity as both astronomical configurations share an intense contrast in summer/winter solar input.

Similarly to Aqua90, surface temperatures in the winter hemisphere remain largely above freezing (because of the heat release by the ocean, not shown) and temperature gradient are very weak throughout the troposphere. In contrast with Aqua90, temperature gradients are also weak in the summer hemisphere, only  $\sim 10$  K (Fig. 14, bottom left, to be compared with Fig. 4, upper left).

As a consequence, the synoptic scale activity is weak in both hemispheres as are surface winds in the midlatitudes. As in Aqua90, a Hadley circulation develops with an upper flow from the summer to the winter hemisphere (not shown). It is weaker than in Aqua90 (by a factor 2) as expected from the smaller meridional gradient of incoming solar radiation (see Fig. 1). This cell drives a mirror overturning cell in the ocean (Held, 2001). The mirror ocean–atmosphere overturning circulations explain nearly all of the northward OHT and AHT found in January (Fig. 14, bottom right). Energy transports in both fluids and oceanic MOC are, directly or indirectly, driven by the thermally direct seasonal Hadley circulation which is itself forced by meridional contrasts in solar heating.

To the extent that this forcing is linear, the canceling of seasonal contrasts in incoming solar radiation (the annual mean meridional profile is “flat”) leads to a vanishing of the annual mean Hadley circulation, and hence of its AHT and of the oceanic MOC and associated OHT. Indeed, the energy transports in July (not shown) are the opposite of those observed in January and the annual mean values are only a small residual (Fig. 14, top right).

Indeed, the annual mean AHT is almost exclusively due to transports by midlatitudes eddies (not shown) but this contribution is four times smaller than in Aqua90 (0.5 PW compared to 2 PW in Fig. 9, top). Nonetheless, the mean energy transports are equatorward, down the (weak) mean temperature gradients.

## References

- Abe, Y., Abe-Ouchi, A., Sleep, N.H., Zahnle, K.J., 2011. Habitable zone limits for dry planets. *Astrobiology* 11, 443–460.
- Adcroft, A., Campin, J., Hill, C., Marshall, J., 2004. Implementation of an atmosphere–ocean general circulation model on the expanded spherical cube. *Mon. Weather Rev.* 132, 2845–2863.
- Armstrong, J.C., Barnes, R., Domagal-Goldman, S., Breiner, J., Quinn, T.R., Meadows, V.S., 2014. Effects of extreme obliquity variations on the habitability of exoplanets. *Astrobiology* 14, 277–291.
- Bretherton, F.P., 1966. Critical layer instability in baroclinic flows. *Q. J. R. Meteor. Soc.* 92, 325–334.
- Campin, J.M., Marshall, J., Ferreira, D., 2008. Sea ice–ocean coupling using a rescaled vertical coordinate  $z^*$ . *Ocean Modell.* 24, 1–14.
- Carpenter, R.L., 1964. Study of Venus by CW radar. *Astron. J.* 69, 2–11.
- Carter, J.A., Winn, J.N., 2010. Empirical constraints on the oblateness of an exoplanet. *Astrophys. J.* 709, 1219–1229.
- Correia, A.C.M., Laskar, J., 2011. Tidal Evolution of Exoplanets. Exoplanets. University of Arizona Press.
- Cowan, N.B., Voigt, A., Abbot, D.S., 2012. Thermal phases of Earth-like planets: Estimating thermal inertia from eccentricity, obliquity, and diurnal forcing. *Astrophys. J.* 757. <http://dx.doi.org/10.1088/0004-637X/757/1/80>, 80 (13 pages).
- Cunha, D., Correia, A.C.M., Laskar, J., 2014. Spin evolution of Earth-sized exoplanets, including atmospheric tides and core–mantle friction. *Int. J. Astrobiol.*, 1–22.
- Czaja, A., Marshall, J.C., 2006. The partitioning of poleward heat transport between the atmosphere and ocean. *J. Atmos. Sci.* 63, 1498–1511.
- Donnadieu, Y., Ramstein, G., Fluteau, F., Besse, J., Meert, J., 2002. Is high obliquity a plausible cause for neoprotozoic glaciations. *Geophys. Res. Lett.* 29, 1–4.
- Enderton, D., Marshall, J., 2009. Explorations of atmosphere–ocean–ice climates on an aqua-planet and their meridional energy transports. *J. Atmos. Sci.* 66, 1593–1611.



- Ferreira, D., Marshall, J., Campin, J.M., 2010. Localization of deep water formation: Role of atmospheric moisture transport and geometrical constraints on ocean circulation. *J. Climate* 23, 1456–1476.
- Ferreira, D., Marshall, J., Rose, B., 2011. Climate determinism revisited: Multiple equilibria in a complex climate model. *J. Climate* 24, 992–1012.
- Gaidos, E., Williams, D.M., 2004. Seasonality on terrestrial extrasolar planets: Inferring obliquity and surface conditions from infrared light curves. *New Astron.* 10, 67–77.
- Gent, P.R., McWilliams, J.C., 1990. Isopycnic mixing in ocean circulation models. *J. Phys. Oceanogr.* 20, 150–155.
- Green, J.S., 1970. Transfer properties of the large-scale eddies and the general circulation of the atmosphere. *Q. J. R. Meteor. Soc.* 96, 157–185.
- Held, I., 2000. The general circulation of the atmosphere. In: Woods Hole Oceanographic Institution Geophysical Fluid Dynamics Program, Woods Hole Oceanographic Institution, p. 54.
- Held, I., 2001. The partitioning of the poleward energy transport between the tropical ocean and atmosphere. *J. Atmos. Sci.* 58, 943–948.
- Hoffman, P.F., Schrag, D.P., 2002. The snowball Earth hypothesis: Testing the limits of global change. *Terra Nova* 14, 129–155.
- Hoffman, P.F., Kaufman, A.J., Halverson, G.P., Schrag, D.P., 1998. A neoproterozoic Snowball Earth. *Science* 281, 1342–1346.
- Jenkins, G.S., 2000. Global climate model high-obliquity solutions to the ancient climate puzzles of the faint-young Sun paradox and low-altitude proterozoic glaciation. *J. Geophys. Res.* 105.
- Jenkins, G.S., 2003. Gcm greenhouse and high-obliquity solutions for early proterozoic glaciation and middle proterozoic warmth. *J. Geophys. Res.* 108.
- Kasting, J.F., Kopparapu, R., Ramirez, R.M., Harman, C.E., 2013. Remote life detection criteria, habitable zone boundaries, and the frequency of Earthlike planets around m and late-k stars. *Proc. Natl. Acad. Sci.* 111, 12641–12646.
- Kirschvink, J.L., 1992. Late Proterozoic Low-Latitude Global Glaciation: The Snowball Earth. *The Proterozoic Biosphere: A Multidisciplinary Study*. Cambridge Univ. Press, New York.
- Klinger, B.A., Marshall, J., Send, U., 1996. Representation of convective plumes by vertical adjustment. *J. Geophys. Res.* C8, 18,175–18,182.
- Laskar, J., Robutel, P., 1993. The chaotic obliquity of the planets. *Nature* 361, 606–612.
- Laskar, J., Joutel, F., Robutel, P., 1993. Stabilization of the Earth's obliquity by the Moon. *Nature* 361, 615–617.
- Marshall, J., Adcroft, A., Hill, C., Perelman, L., Heisey, C., 1997. A finite-volume, incompressible Navier stokes model for studies of the ocean on parallel computers. *J. Geophys. Res.* 102, 5753–5766.
- Marshall, J., Adcroft, A., Campin, J.M., Hill, C., White, A., 2004. Atmosphere–ocean modeling exploiting fluid isomorphisms. *Mon. Weather Rev.* 132, 2882–2894.
- Marshall, J., Ferreira, D., Campin, J., Enderton, D., 2007. Mean climate and variability of the atmosphere and ocean on an aquaplanet. *J. Atmos. Sci.* 64, 4270–4286.
- Molteni, F., 2003. Atmospheric simulations using a GCM with simplified physical parametrizations. I: Model climatology and variability in multi-decadal experiments. *Climate Dyn.* 64, 175–191.
- North, G.R., Cahalan, R.F., Coakle Jr., James A., 1981. Energy balance climate models. *Rev. Geophys. Space Phys.* 19, 91–121.
- Pauluis, O., 2004. Boundary layer dynamics and cross-equatorial Hadley circulation. *J. Atmos. Sci.* 61, 1161–1173.
- Pierrehumbert, R.T., Abbot, D.S., Voigt, A., Koll, D., 2011. Climate of the neoproterozoic. *Annu. Rev. Earth Planet. Sci.* 39, 417–460.
- Poulsen, C.J., Jacob, R.L., 2004. Factors that inhibit Snowball Earth simulation. *Paleoceanography* 19. <http://dx.doi.org/10.1029/2004PA001056>, PA4021 (11 pages).
- Poulsen, C.J., Pierrehumbert, R.T., Jacob, R.L., 2001. Impact of ocean dynamics on the simulation of the neoproterozoic “Snowball Earth”. *Geophys. Res. Lett.* 28, 1575–1578.
- Redi, M.H., 1982. Oceanic isopycnal mixing by coordinate rotation. *J. Phys. Oceanogr.* 12, 1154–1158.
- Rose, B.E., Ferreira, D., 2013. Ocean heat transport and water vapor greenhouse in a warm equable climate: A new look at the low gradient paradox. *J. Climate* 26, 2117–2136.
- Rose, B.E., Marshall, J., 2009. Ocean heat transport, sea ice and multiple climatic states: Insights from energy balance models. *J. Atmos. Sci.* 66, 2828–2843.
- Seager, S., 2014. The future of spectroscopic life detection on exoplanets. *Proc. Natl. Acad. Sci.* 111, 12634–12640. <http://dx.doi.org/10.1073/pnas.1304213111>.
- Seager, R., Battisti, D.S., Yin, J., Gordon, N., Naik, N., Clement, A.C., Cane, M.A., 2002. Is the Gulf stream responsible for Europe's mild winters? *Q. J. R. Meteor. Soc.* 128, 2563–2586.
- Shapiro, I.I., 1967. Resonance rotation of Venus. *Science* 157, 423–425.
- Smith, S.K., 2007. The geography of linear baroclinic instability in Earth's oceans. *J. Marine Res.* 65, 655–683.
- Spiegel, D.S., Menou, K., Scharf, C.A., 2009. Habitable climates: The influence of obliquity. *Astrophys. J.* 691, 596–610.
- Stone, P.H., 1972. A simplified radiative-dynamical model for the static stability of rotating atmospheres. *J. Atmos. Sci.* 29, 405–418.
- Touma, J., Wisdom, J., 1993. The chaotic obliquity of Mars. *Science* 259, 1294–1297.
- Trenberth, K.E., Caron, J.M., 2001. Estimates of meridional atmosphere and ocean heat transports. *J. Climate* 14, 3433–3443.
- Williams, D.M., Kasting, J.F., 1997. Habitable planets with high obliquities. *Icarus* 2, 254–267.
- Williams, D.M., Pollard, D., 2003. Extraordinary climates of Earth-like planets: Three-dimensional climate simulations at extreme obliquity. *Int. J. Astrobiol.* 2, 1–19.
- Winton, M., 2000. A reformulated three-layer sea ice model. *J. Atmos. Ocean. Technol.* 17, 525–531.
- Zsom, A., Seager, S., de Wit, J., Stamenkovic, V., 2013. Toward the minimum inner edge distance of the habitable zone. *Astrophys. J.* 778, 109.